

Numerical study on aerodynamic and aeroacoustics characteristics of sinusoidal wavy square cylinders

Hongyin Bao (鲍鸿音),¹ Lian Gan (干联),^{2, a)} and Yu Liu (刘宇)^{1, b)}

¹⁾*Department of Mechanics and Aerospace Engineering, Southern University of Science and Technology, Shenzhen, Guangdong 518055, China*

²⁾*Department of Engineering, Durham University, Durham, DH1 3LE, United Kingdom*

(Dated: 26 September 2024)

This paper numerically investigates the influences of amplitude and wavelength of sinusoidal wavy square cylinders on aerodynamic performance and noise reduction by large eddy simulation along with the Ffowcs Williams-Hawkings equation. The results show that the mean drag, lift fluctuation and far-field noise of wavy cylinders are all reduced compared to the straight counterpart. The far-field noise of wavy cylinders varies monotonically with amplitude in specific range but not with wavelength. The case with the largest amplitude demonstrates a significant tonal noise reduction of 47 dB/Hz, while a tonal noise reduction of 23 dB/Hz is observed for the case with the largest wavelength. To explore the mechanisms of noise reduction, the characteristics of flow field are analysed. It is found that wavy cylinders attenuate the transverse oscillation of shear layer and produce more three-dimensional coherent structures in the wake. The wake region is significantly extended due to the delayed vortex shedding, and the mutual interaction between shear layers is remarkably weakened along the entire span. The spanwise coherence is attenuated in a similar way. These lead to the suppression of wall pressure fluctuations and turbulence fluctuations in the wake, which are closely related to far-field noise radiation.

I. INTRODUCTION

Turbulent flows around bluff bodies such as circular, square, or triangular cylinders are prevalent in many industrial applications. Aerodynamic noise generated from bluff bodies has been widely concerned in recent years. The square cylinder, a common type of bluff body, is frequently used in applications like high-speed train pantographs¹, aircraft landing gear frames² and skyscrapers³. Minimising aerodynamic noise is therefore practically useful. Current aerodynamic noise reduction methods for flow over bluff bodies can be broadly categorised into active and passive methods. Active methods, such as plasma⁴ and air blowing and suction⁵, usually require external energy input to disturb the boundary layer in a controlled manner, thereby achieving noise reduction. In contrast, passive control methods do not consume energy and therefore are extensively applied in practice. Common techniques include serrated structures⁶⁻⁸, porous coatings⁹⁻¹¹, and shape modifications¹².

Altering cylinder geometry from straight to wavy shape is one of the simple passive methods for aerodynamic noise reduction. Extensive numerical and experimental investigations have been conducted on spanwisely wavy circular cylinders, focusing on the overall noise reduction and the associated change of flow characteristics in the near wake region in the subcritical regime. A range of wavelengths $\lambda/D_m \in [1.136, 7.57]$ was studied by Lam and Lin¹³ and Lin et al.¹⁴, where D_m is the mean cylinder diameter. Significant reduction in the time-mean drag and fluctuating lift are shown to be achievable at specific wavelengths. Bai et al.¹⁵ applied three-dimensional (3-D) proper orthogonal decomposition (POD)

method to the near-wake flow structure behind wavy circular cylinders with $\lambda/D_m = 1.89, 3.79$ and 6.06 . They found that for wavy cylinders energy content is shifted from the first two POD modes to higher modes. In terms of noise level, Zhang et al.¹⁶ observed a reduction of far-field noise by 6.7 dB from a cylinder of wavelength $\lambda/D_m = 0.69$ and wave amplitude $A/D_m = 0.0345$. Measurements conducted by Bai et al.¹² in an acoustic wind tunnel reported a substantial reduction in far-field tonal and broadband noise, particularly for cylinders of $\lambda/D_m = 1.8$ and 6.0 .

Studies on cylinders of other cross-sectional shapes are relatively sparse. In the case of a square cylinder with a single wavy surface facing normally to the incoming flow, Bearman and Owen¹⁷ demonstrated a drag coefficient reduction of up to 34% for cylinders of $\lambda/h = 5.6$, where h is the height of thin plates. This non-dimensional wavelength is close to the critical value $\lambda/D = 5.22$, where D is the diameter of straight square cylinders, and is associated with the so-called mode A instability¹⁸, a 3-D instability at low Reynolds numbers. Particle Image Velocimetry (PIV) measurements and dynamic mode decomposition (DMD) analysis by Zheng et al.¹⁹ revealed that a square cylinder having a wavy windward surface suppresses vortex shedding. Large eddy simulation (LES) studies of this type of cylinders with $\lambda/D = 5.6$ by Zhanget al.²⁰ showed a reduction up to 27% and 98% for the mean drag and lift fluctuation, respectively, confirming the highly sensitive wavelength for mode A instability in the subcritical flow regime. Experimental investigations conducted by Dobre et al.²¹ on a wavy cylinder with $\lambda/D = 2.4$ demonstrated a remarkable 78% decrease in turbulent intensity. Additionally, Antiohos and Thorpe²² utilised LES to study the same model as in Dobre's experiment, and confirmed significant reductions in mean drag and lift fluctuations. It is worth mentioning that this wavelength ($\lambda/D = 2.4$) coincides with the mode A wavelength at the same Reynolds number²³. Darekar and Sherwin²⁴ conducted a stability study using a spectral el-

^{a)}Corresponding author: lian.gan@durham.ac.uk

^{b)}Corresponding author: liuy@sustech.edu.cn

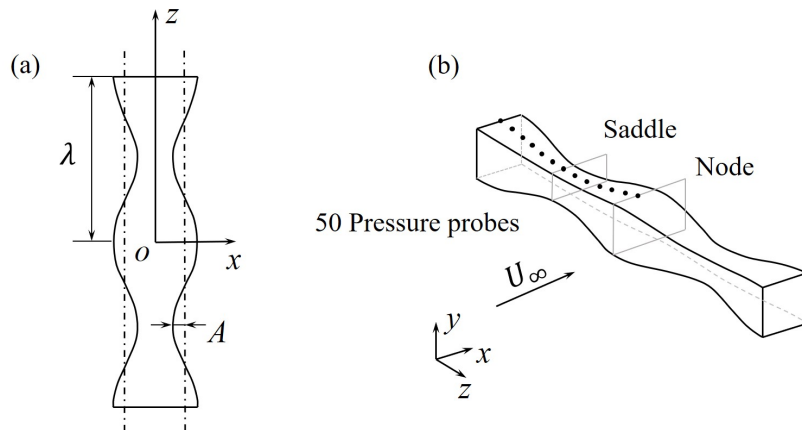


FIG. 1. Schematic of cylinder geometry: (a) top view and (b) isometric view. The dark dots in (b) indicate the 50 pressure probes for the calculations of spanwise coherence and far-field noise, which are evenly distributed along the curve of $x = 0$, $y = D(z)/2$ and $0 \leq z \leq \lambda$.

ement solver on square cylinders with spanwisely wavy surfaces on the windward (stagnation) and leeward sides, for $\lambda/D \in [0, 11]$ at low Reynolds numbers from 10 to 150. Their findings showed that Kármán vortex shedding is suppressed in the case of $\lambda/D \approx 5.6$. Lin et al.²⁵ studied square prisms having a pair of sinusoidally wavy surfaces on opposite sides while the other two surfaces remain flat at $Re = 22000$. They found a more pronounced reduction in the mean drag and lift fluctuations when a flat surface faces normally to the incoming flow. In the context of noise reduction, Liu et al.²⁶ employed both numerical and experimental methods to investigate square cylinders with front and rear wavy surfaces of various amplitudes at $Re = 82000$, and achieved a maximum noise reduction of 36 dB.

To the best of the authors' knowledge, although flow characteristics in the near wake behind square cylinders having either a single or a pair of wavy surfaces have been well documented, the associated directional sensitivity of noise reduction effect is limited. In practice, as the incoming flow direction changes, the effectiveness of noise reduction can be greatly varied. This inspires the current study to look at square cylinders with waviness on all the four surfaces, aiming to diminish the effect of flow direction on noise reduction. Numerical simulations are applied to investigate the flow characteristics and hence the aerodynamic noise. Section II provides a concise description of the cylinder geometry and the computational setup, along with a grid independence check and a validation of the numerical model. In Sec. III, noise reduction effects and mechanisms are discussed. The study concludes in Sec. IV with a summary of findings.

II. NUMERICAL METHODOLOGY

A. Cylinder geometry

The geometry of the wavy square cylinder is presented in Fig. 1, where sinusoidal wavy surfaces are applied to all sides.

The sectional side length $D(z)$ of all the four surfaces varies synchronously as a function of the spanwise coordinate z and is defined as

$$D(z) = D_m + 2A \cos\left(\frac{2\pi z}{\lambda}\right), \quad (1)$$

where D_m denotes the average side length; λ and A represent the wavelength and wave amplitude, respectively. 'Node section' refers to cross sections at wave peaks of D_{max} , and 'saddle section' at wave troughs of D_{min} . We investigate a straight cylinder (Case 0) and six wavy cylinders including four wavelengths and three amplitudes. All the test cases are summarised in Table I. We aim for a constant D_m based Re , which will be defined below, and the spanwise length L_z varies with λ . The chosen $L_z (\geq 4D_m)$ exceeds the recommended minimum spanwise dimension of the computational domain (i.e., $L_z = 2D_m$) in order to ensure satisfactory accuracy for spanwise velocity correlation²⁷.

TABLE I. Parameters of the test cases.

Case #	0	1	2	3	4	5	6
λ/D_m	∞	2.4	2.4	2.4	2.4	4.0	5.6
A/D_m	0	0.10	0.15	0.20	0.25	0.15	0.15
L_z/D_m	4.0	4.8	4.8	4.8	4.8	4.0	5.6

B. Computational domain and boundary conditions

Fig. 2(a) outlines the computational domain in the x - y plane. The inlet surface is at $x = -10D_m$, where a constant and uniform velocity U_∞ is applied. The pressure outlet condition is applied on the outlet surface at $x = 20D_m$, where pressure is set to zero. Along the y -direction, symmetry boundary condition is applied to the top and the bottom surfaces located

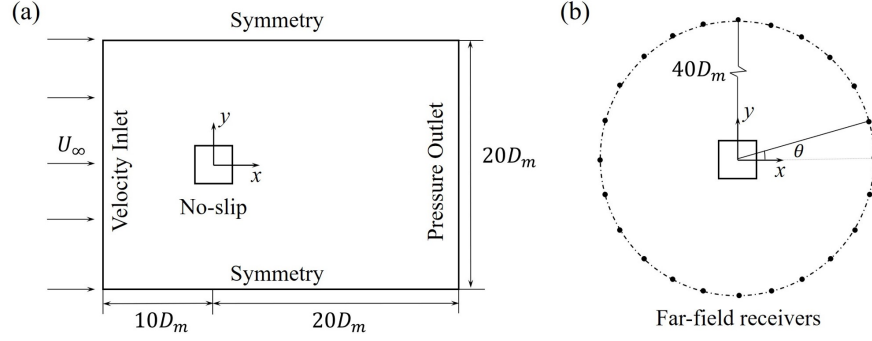


FIG. 2. Schematic of the computational details: (a) computational domain and boundary conditions and (b) the locations of far-field receivers.

at $\pm 10D_m$ away from the cylinder centreline. The computational domain size in the x - y plane is larger than that adopted in Sohankar et al.²⁸, which is deemed sufficient for reasonably accurate flow information. Periodic boundary condition is applied on the domain surfaces in the z -direction at $z = \pm L_s/2$, where L_s is the spanwise length. Standard no-slip boundary condition is applied to the cylinder surface. Flow condition is set at constant $Re = U_\infty D_m / \nu = 2.2 \times 10^4$, where the incoming flow velocity $U_\infty = 13.2$ m/s, $D_m = 25$ mm, and ν is the kinematic viscosity of air in room temperature. For the calculation of far-field noise, the Ffowcs Williams-Hawking (FW-H) integration surface is placed on the square cylinder. The far-field receivers are placed in the $z = 0$ plane at a constant radius of $R = 40D_m$ and an interval of $\Delta\theta = 15^\circ$ resulting in 24 receivers in total, as shown in Fig. 2 (b).

C. LES model and the FW-H equation

We perform wall-adapting local eddy-viscosity model (LES-WALE)²⁹ along with the FW-H equation to investigate the influence of wave amplitude and wavelength on the near-wake flow characteristics and aerodynamic noise. Large eddy simulation aims to solve the unsteady Navier-Stokes equation by segregating large-scale vortices and small-scale vortices. Large-scale vortices are directly solved, while a sub-grid scale (SGS) model is employed to model the small-scale vortices. The filtered incompressible LES equations are

$$\frac{\partial \bar{u}_i}{\partial x_i} = 0, \quad (2)$$

$$\frac{\partial \bar{u}_i}{\partial t} + \frac{\partial \bar{u}_i \bar{u}_j}{\partial x_j} = -\frac{1}{\rho} \frac{\partial \bar{p}}{\partial x_i} + \frac{\partial}{\partial x_j} \left[\nu \left(\frac{\partial \bar{u}_i}{\partial x_j} + \frac{\partial \bar{u}_j}{\partial x_i} \right) + \tau_{ij} \right], \quad (3)$$

where x_i represents the Cartesian coordinates adopted in this study, \bar{u} the filtered velocity, and \bar{p} the filtered pressure. The SGS stress tensor is given by $\tau_{ij} = \bar{u}_i \bar{u}_j - \bar{u}_i \bar{u}_j$, and should be modeled with the WALE model²⁹ based on an eddy-viscosity assumption,

$$\tau_{ij} - \frac{1}{3} \tau_{kk} \delta_{ij} = 2\nu_t \bar{S}_{ij}, \quad (4)$$

$$\bar{S}_{ij} = \frac{1}{2} (\bar{g}_{ij} + \bar{g}_{ji}), \quad (5)$$

where \bar{S}_{ij} is the rate of strain tensor; \bar{g}_{ij} is the velocity gradient tensor defined as $\bar{g}_{ij} = \partial \bar{u}_i / \partial x_j$; ν_t is SGS viscosity, which is defined as follow:

$$\nu_t = (C_w \Delta)^2 \frac{(S_{ij}^d S_{ij}^d)^{3/2}}{(\bar{S}_{ij} \bar{S}_{ij})^{5/2} + (S_{ij}^d S_{ij}^d)^{5/4}}, \quad (6)$$

where the model coefficient is taken as $C_w = 0.544$ (a sensitivity test is presented in the Appendix), Δ is the filtration scale, and S_{ij}^d is the traceless symmetric part of the square of the velocity gradient tensor, $S_{ij}^d = \frac{1}{2} (\bar{g}_{ij}^2 + \bar{g}_{ji}^2) - \frac{1}{3} \delta_{ij} \bar{g}_{kk}^2$.

Spatial discretisation utilises the bounded-central-differencing scheme with an upwind blending factor to ensure a balance between accuracy and robustness. The second-order implicit scheme (Backward Differentiation Formula) is applied for temporal discretisation, which is expressed as,

$$\frac{\partial \phi}{\partial t} = \frac{3\phi^{n+1} - 4\phi^n + \phi^{n-1}}{2\Delta t}, \quad (7)$$

The Hybrid Gauss-Least Squares method is used for gradient calculation, which combines the Green-Gauss and Least Squares gradient method to balance the accuracy and efficiency. Numerical simulations are implemented in the commercial software STAR-CCM+. The entire simulation lasts for 0.6 s, which corresponds to approximately 50 vortex shedding cycles, with a transient time step of 5×10^{-6} s for all cases.

Based on the flow-field data obtained, the far-field noise is predicted by the FW-H module with Farassat 1A formulation in STAR-CCM+. On the basis of Lighthill and Curle acoustic analogies^{30,31}, Ffowcs Williams and Hawkings³² extended the equations to consider a surface in arbitrary motion, which is expressed as

$$\begin{aligned} \left(\frac{\partial^2}{\partial t^2} - c_0^2 \nabla^2 \right) [H(f) \rho'] &= \frac{\partial^2}{\partial x_i \partial x_j} [T_{ij} H(f)] \\ &- \frac{\partial}{\partial x_i} \{ [pn_i + \rho u_i (u_n - v_n) - \tau_{ij} n_j] \delta(f) \} \\ &+ \frac{\partial}{\partial t} [\rho_0 v_n + \rho (u_n - v_n) \delta(f)], \end{aligned} \quad (8)$$

TABLE II. Comparison of time-averaged drag coefficient and vortex shedding Strouhal number of the straight square cylinder among the three meshes and previous numerical and experimental results.

Methods	Cases	Grid	Re	\bar{C}_D	St
LES	Coarse	$26,900 \times 80$	2.2×10^4	2.29	0.132
	Medium	$52,100 \times 80$	2.2×10^4	2.21	0.132
	Fine	$76,900 \times 80$	2.2×10^4	2.22	0.132
	Sohankar et al. ²⁸	$185 \times 105 \times 25$	2.2×10^4	2.20	0.127
	Cao and Tamura ³³	$300 \times 300 \times 81$	2.2×10^4	2.21	0.132
DNS	Trias et al. ²⁷	$1272 \times 1174 \times 216$	2.2×10^4	2.18	0.132
Exp.	Luo et al. ³⁴	–	2.2×10^4	2.21	0.130
	Norberg ³⁵	–	1.3×10^4	2.16	0.132

where c_0 is the speed of sound and ρ' is the density fluctuation. The right hand side of the equation comprises three terms: the first term represents a quadrupole source resulting from turbulence in the flow field, which is expressed by $T_{ij} = \rho u_i u_j + (p - c_0^2 \rho') - \tau_{ij}$, i.e., the Lighthill stress tensor; the second term is a dipole source arising from unsteady forces applied on the body, and the third term is the monopole source associated with unsteady mass flux. The Navier-Stokes equation can be treated in incompressible form, and the quadrupole noise is negligible compared to the dipole noise at low Mach number ($Ma \ll 0.3$)³⁶. Lockard et al.² found that there were only minor differences between solid and permeable surfaces when predicting the noise from circular cylinders at low mach numbers. Therefore, the impermeable surface method is a suitable choice in the present study. When applying the FW-H integration over a stationary solid surface, the monopole term becomes zero. Therefore only the dipole noise is calculated in Eq. (8).

Statistical flow-field data and acoustic pressure results are sampled over a time period from 0.2 s to 0.6 s, capturing 30 vortex shedding cycles. Acoustic pressure signals at the far-field receivers are transformed into power spectral density (PSD), ϕ_{pp} , using Welch's method. The dataset is partitioned into three segments with a 50% overlap. The PSD is then converted into decibels as

$$\text{PSD (dB/Hz)} = 10 \log_{10} \left(\frac{\phi_{pp}}{p_{ref}^2} \right), \quad (9)$$

where the reference pressure $p_{ref} = 2 \times 10^{-5}$ Pa. The overall sound pressure level (OASPL) is defined as the integral of PSD over the frequency range from 20 Hz to 20000 Hz.

D. Grid independence and validation

1. Influence of 2-D planar grid resolution

Fig. 3 shows the structured hexahedral grid adopted in this study. The whole domain is divided into nine blocks. The

O-block is set around the cylinder. Inside the O-block, the grids are clustered around the cylinder and extends outward at a rate of 1.1, which ensures $y^+ < 1$. The averaged values of x^+ , y^+ , and z^+ are approximately 9, 0.25 and 31, respectively, meeting the requirements of wall-resolved LES³⁷. The maximum x^+ and z^+ values, 27 and 95, occur near the frontal corners. Although the maximum z^+ is larger than the requirement of wall-resolved LES, the near-wall grid resolution is reasonably sufficient for LES since the boundary layer attached on the frontal surface remains laminar³³. Around the O-block, in the dense region, a bi-geometric method is employed, where the grids extend from the region boundary toward the centerline with a growth rate of 1.1; in the coarse region, non-uniform grids extend along the x - and y -axes with the same growth rate. In total 80 grids are uniformly distributed along the z -direction²⁶. To accelerate simulations, results from steady-state shear stress transfer (SST) $k-\omega$ model are used as initial conditions for transient simulations. The non-dimensional time step $\Delta t^* = \Delta t U_\infty / D_m = 0.0032$ satisfies $\text{CFL} = U_\infty \Delta t / \Delta x < 1$ in most region of the computational domain.

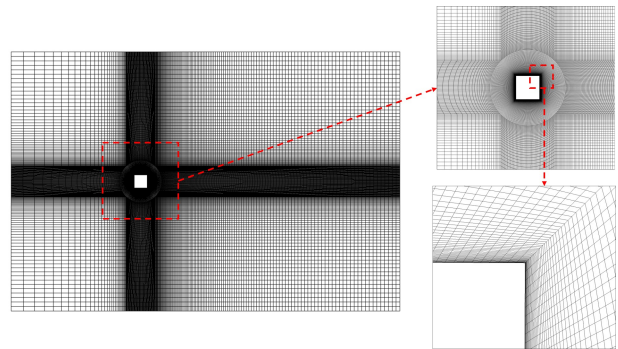


FIG. 3. Grid distribution in the $z = 0$ plane.

The wake of the straight cylinder is close to a two-dimensional (2-D) flow field, and thus the straight cylinder case was selected to investigate the influence of planar grid resolution on the numerical results. A grid sensitivity analy-

sis was performed in terms of time-averaged drag coefficient \bar{C}_D and vortex shedding Strouhal number St for the straight square cylinder, as shown in Table II. Together with lift coefficient C_L , the aerodynamic variables are defined as

$$C_D = \frac{F_D}{0.5\rho U_\infty^2(L_s D_m)}, \quad C_L = \frac{F_L}{0.5\rho U_\infty^2(L_s D_m)}, \quad (10a)$$

$$St = \frac{f_{vs} D_m}{U_\infty}, \quad (10b)$$

where F_D and F_L are the drag and lift forces, respectively, f_{vs} is the vortex shedding frequency determined from the lift coefficient spectrum. Time-averaged quantities are calculated over 30 vortex shedding cycles after the quasi-steady state is reached. As shown in Table II, the values of \bar{C}_D and St from the medium mesh demonstrate sufficient accuracy compared to the high-fidelity direct numerical simulation (DNS) and experimental results, as well as other LES cases.

The distance between the cylinder centre and the location where $\bar{u} = 0$ defines the recirculation bubble length L_r ³⁹, which can be obtained from the profile of mean streamwise velocity as shown in Fig. 4(a). It can be observed that L_r is not sensitive to the grid number in the x - y plane. At a downstream location of $x/D_m > 3$, the \bar{u} values of the Coarse, Medium and Fine meshes are all close to those of the DNS²⁷ and LES²⁸ results. Fig. 4(b) shows the profile of the root-mean square (rms) of transverse velocity. It is found that the location and magnitude of peak v_{rms} are close to the LES results of Sotherankar et al.²⁸. In general, the medium mesh case exhibits a good agreement with the DNS, LES and experimental results. Therefore, the Medium mesh with 52,100 elements in the x - y plane is sufficient to resolve the 2-D flow field and is adopted in the present study.

2. Influence of spanwise grid resolution

In order to sufficiently resolve the flow field along the spanwise direction, the most wavy case (Case 3) is chosen to investigate the influence of spanwise grid resolution. A number of 52,100 elements are set in the x - y plane, which has been proved to produce accurate results for 2-D wake, whereas in the z -direction the grid number varies from 56 to 136. Table III shows that the spanwise resolution does not much affect on the drag coefficient. The recirculation bubble length L_r grows slightly with increasing grid number. Therefore, 96 spanwise grid points are selected for subsequent analysis by considering a balance between accuracy and computational cost. For the wavy cylinder with different wavelengths, the spanwise grid points are set as $N_z = 96, 80, \text{ and } 112$ for Cases 2, 5, and 6, respectively.

3. Far-field noise validation

A direct comparison of radiated far-field noise among the test cases is difficult since the far-field noise PSD is associated with the spanwise length L_z , which however varies in this

TABLE III. Comparison of time-averaged drag coefficient and spanwise averaged recirculation bubble length of the wavy square cylinder (Case 3) among the three meshes.

Cases	Grid	Re	\bar{C}_D	L_r/D_m
Coarse	52,100 × 56	2.2×10^4	1.54	3.66
Medium	52,100 × 96	2.2×10^4	1.53	3.71
Fine	52,100 × 136	2.2×10^4	1.53	3.76

study to ensure the same length of two wavelengths for all cases. Consequently, for a meaningful and fair comparison between the simulated and experimental data, the predicted noise PSD should be normalised in the spanwise direction. This is achieved by employing an acoustic correction method proposed by Seo and Moon⁴⁰ as follows,

$$\text{PSD}(f) = \text{PSD}_s(f) + \text{PSD}_c \quad (11)$$

with the correction term

$$\text{PSD}_c = \begin{cases} 10 \log_{10} \left(\frac{L_e}{L_s} \right) & \sqrt{\pi} L_c \leq L_s; \\ 10 \log_{10} \left(\frac{L_c}{L_s} \right) + 10 \log_{10} \left(\frac{\sqrt{\pi} L_e}{L_s} \right) & L_s \leq \sqrt{\pi} L_c \leq L_e; \\ 20 \log_{10} \left(\frac{L_e}{L_s} \right) & L_e \leq \sqrt{\pi} L_c. \end{cases} \quad (12)$$

In equation (12), L_e and L_s are the spanwise lengths of experiment and simulation, respectively, and L_c represents the coherence length which can be obtained by a Gaussian fitting of the coherence function⁴⁰, i.e.,

$$C_{xy}(f) = \frac{|P_{xy}(f)|^2}{P_{xx}(f)P_{yy}(f)}, \quad (13)$$

with the Gaussian fitting form

$$C_{xy}(\Delta z) = \exp(-\Delta z^2/L_c^2), \quad (14)$$

where P_{xy} is the cross-PSD of two pressure signals at the spanwise locations of $z = 0$ and $z = \Delta z$, and P_{xx}, P_{yy} are auto-PSDs of the same signal.

A total of 50 surface pressure probes are placed along half span of the square cylinder as depicted in Fig. 1(b). The spectrum of coherence function is obtained through Eq. (13). Fig. 5 highlights a remarkable coherence of surface pressure fluctuation at $St = 0.13$, in contrast to the lower coherence at other frequencies. Following the approach by Seo and Moon⁴⁰, the calculation of coherence length L_c is performed at an ‘interest’ frequency. For the flow around a cylinder, particular attention should be given to the vortex shedding frequency which is also significant to far-field noise. Therefore, L_c is calculated at $St = 0.13$ and is used for the correction in Eq. (12). For the straight square cylinder, the computed L_c at $St = 0.13$ is $17.5D_m$, close to the result of Jacob and Bhattacharya⁴², and is larger than the simulation spanwise

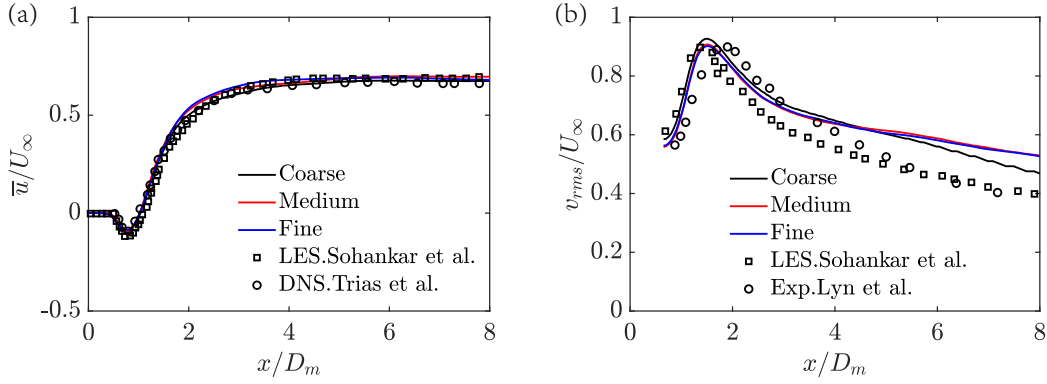


FIG. 4. Profiles of time and spanwise averaged streamwise velocity \bar{u} (a) and rms transverse velocity v_{rms} (b) for the straight cylinder with different grid resolutions. Previous DNS (Trias et al.²⁷, $Re = 22000$), LES (Sohankar et al.²⁸, $Re = 22000$) and experimental (Lyn et al.³⁸, $Re = 21400$) data of the straight cylinder are presented for comparison.

TABLE IV. Spanwise coherence lengths and aerodynamic variables \bar{C}_D , $C_{L,rms}$ for difference square cylinders of Cases 0–6. $L_e = 20D_m$.

Case #	Shape	L_c	Correction	\bar{C}_D	$C_{L,rms}$
0	Straight	$17.5D_m$	$L_s \leq \sqrt{\pi}L_c \leq L_e$	2.22	1.52
1	$\lambda/D_m = 2.4, A/D_m = 0.10$	$11.2D_m$	$L_s \leq \sqrt{\pi}L_c \leq L_e$	2.09	0.89
2	$\lambda/D_m = 2.4, A/D_m = 0.15$	$9.9D_m$	$L_s \leq \sqrt{\pi}L_c \leq L_e$	1.80	0.43
3	$\lambda/D_m = 2.4, A/D_m = 0.20$	$0.6D_m$	$\sqrt{\pi}L_c \leq L_s$	1.58	0.05
4	$\lambda/D_m = 2.4, A/D_m = 0.25$	$0.9D_m$	$\sqrt{\pi}L_c \leq L_s$	1.53	0.05
2	$\lambda/D_m = 2.4, A/D_m = 0.15$	$11.2D_m$	$L_s \leq \sqrt{\pi}L_c \leq L_e$	1.80	0.43
5	$\lambda/D_m = 4.0, A/D_m = 0.15$	$15.8D_m$	$L_s \leq \sqrt{\pi}L_c \leq L_e$	2.05	0.69
6	$\lambda/D_m = 5.6, A/D_m = 0.15$	$11.7D_m$	$L_s \leq \sqrt{\pi}L_c \leq L_e$	1.82	0.28

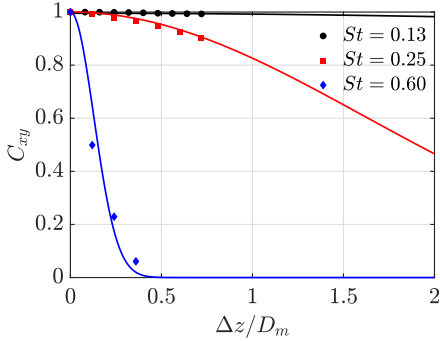


FIG. 5. The coherence function C_{xy} for the straight square cylinder at three frequencies. Symbols and lines indicate the numerical results and Gaussian fitting, respectively.

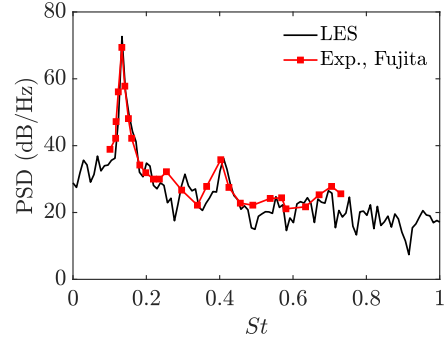


FIG. 6. Comparison of far-field noise PSD between the present numerical simulation and experiment by Fujita⁴¹ ($Re = 18000$) for the straight square cylinder.

the influence of different Reynolds numbers,

$$\overline{p'^2} = \frac{\rho_0^2 U_\infty^6 St^2 C_{L,rms}^2 L_z L_c}{16c_0^2 R^2}. \quad (15)$$

length L_s . The value of L_e is taken as $10D_m$ following the experimental setup by Fujita⁴¹. The overall sound pressure level (OASPL) obtained from Curle's analogy⁴¹ is used to correct

Fig. 6 shows that the corrected noise PSD spectrum is in a

good agreement with the experiment results of Fujita⁴¹. Consequently, the spanwise acoustic correction method will be applied subsequently for the far-field noise prediction of wavy cylinders.

III. RESULTS AND DISCUSSION

A. Aerodynamic and aeroacoustic results

Table IV lists the coherence length L_c , time-averaged drag coefficient \bar{C}_D , and rms lift coefficient $C_{L,rms}$. Notably, all three variables decrease when wavy surfaces are introduced. In particular, for the most wavy Case 4 ($\lambda/D_m = 2.4$, $A/D_m = 0.25$), the reductions of \bar{C}_D and $C_{L,rms}$ are 31% and 97%, respectively, compared to the straight cylinder. \bar{C}_D and $C_{L,rms}$ firstly vary monotonically with the wave amplitude A and then remain nearly unchanged from Case 3 ($\lambda/D_m = 2.4$, $A/D_m = 0.20$). However, \bar{C}_D and $C_{L,rms}$ do not vary monotonically with increasing wavelength λ . For Case 6 ($A/D_m = 0.15$, $\lambda = 5.6D_m$), \bar{C}_D and $C_{L,rms}$ are significantly reduced by 18% and 82%, respectively. The coherence length at the peak frequency given in Table IV is used in Eq. (12) to correct the far-field noise from the simulation length of L_s to the same experiment length of $L_e = 20D_m$.

Fig. 7(a) displays the corrected far-field noise PSD measured by the receiver at $\theta = 90^\circ$ for the wavy cylinders with varying amplitudes ($A/D_m = 0.10$ – 0.25) as well as the straight cylinder as a reference. It can be observed that all cylinders exhibit a prominent tonal peak except Case 3 ($A/D_m = 0.20$) and Case 4 ($A/D_m = 0.25$). For wavy cylinders with $A/D_m = 0.10$, the peak occurs at $St \approx 0.132$ which is close to the straight cylinder. As the amplitude increases to $A/D_m = 0.15$, the Strouhal number of the tonal peak is reduced to $St = 0.128$. More importantly, the tonal peaks of the wavy cylinders are significantly lower than that of the straight cylinder, with a significant reduction of 47 dB/Hz observed for the case of $A/D_m = 0.20$ and $A/D_m = 0.25$. In addition, the broadband noise of wavy cylinders with different amplitudes also exhibits a remarkable reduction relative to that of the straight counterpart.

The far-field noise PSD of wavy cylinders with different wavelengths ($\lambda/D_m = 2.4$ – 5.6) is shown in Fig. 8(a). The wavy cylinders exhibit a reduction in tonal peak compared to the straight cylinder, yet the effect is not as prominent as that of the wave amplitude. For $\lambda/D_m = 4.0$, both the tonal peak and broadband noise do not significantly reduce compared to the straight. However, a significant reduction of 23 dB/Hz is observed when λ/D_m reaches 5.6. Notably, for $\lambda/D_m = 5.6$, the tonal peak occurs at $St = 0.124$, lower than those of other cases. These far-field noise observations are consistent with the $C_{L,rms}$ values presented in Table IV.

Fig. 7(b) and 8(b) depict the far-field OASPL directivities in the $z = 0$ plane, under constant wavelength and amplitude, respectively. Notably, the OASPL of wavy cylinders is reduced in all directions when compared to the straight cylinder, with the maximum reduction observed in the lift direction of $\theta = 90^\circ$. For wavy cylinders with different amplitudes as

shown in Fig. 7(b), a substantial noise reduction is evident for the case of $A/D_m = 0.20$, which is about 36 dB and 18 dB in the lift and drag directions. Fig. 8(b) reveals that when the wavelength increases from $\lambda/D_m = 2.4$ to 4.0, there is a slight noise increase in all directions. However at $\lambda/D_m = 5.6$, a remarkable reduction of OASPL is observed in all directions.

B. Wake flow characteristics

The reductions in tonal, broadband and overall noise originate from the alteration of instantaneous vortex structures in the wake. Fig. 9 illustrates the iso-surface of the second invariant of velocity gradient tensor⁴³, normalised as $Q_n = QD_m^2/U_\infty^2$ and coloured by $\omega_z D_m/U_\infty$. The term Q is defined as

$$Q = \frac{1}{2} (\Omega_{ij}\Omega_{ij} - S_{ij}S_{ij}), \quad (16)$$

where Ω_{ij} is the rotation rate

$$\Omega_{ij} = \frac{1}{2} \left(\frac{\partial u_i}{\partial x_j} - \frac{\partial u_j}{\partial x_i} \right), \quad (17)$$

and S_{ij} is the strain rate

$$S_{ij} = \frac{1}{2} \left(\frac{\partial u_i}{\partial x_j} + \frac{\partial u_j}{\partial x_i} \right). \quad (18)$$

As shown in Fig. 9(a), flow separates along the leading edge of the straight cylinder to form the classical Kármán vortex street. Periodic shedding of Kármán vortices induces pressure fluctuations on the cylinder surfaces, resulting in tonal noise radiation.

Downstream the wavy cylinders, the flow patterns differ obviously from those of the straight cylinder in mainly two aspects. Firstly, vortex shedding is suppressed to some extent. For all wavy cylinders, the separated shear layers elongate and weakly roll up into larger vortices. This is particularly pronounced for Case 3 (c3) and Case 4 (c4), where the length of shear layer before vortex roll-up is significantly increased, and the transverse oscillation of shear layer is notably reduced compared to the straight cylinder, which causes nearly no vortex shedding in the wake. This suggests attenuated wake oscillations and hence surface pressure fluctuations, which accounts for the reduction of tonal noise (nearly no peak) observed in Fig. 7(a). For other wavy cases, although the oscillation of the shear layer is suppressed to some certain extent, reducing the fluctuations in the wake, the spanwise vortex structure can still be found in their wakes. That's why low level peaks still exist in the noise spectrum (Figs. 7a and 8a). Secondly, highly developed 3-D coherent structures can be observed in wavy cases. When the fluid flows around the wavy cylinder, the spanwise motion of the fluid will increase due to the leading edge waviness, which will result in varying length of shear layers before roll-up at different spanwise locations, leading to more complex 3-D vortex structures in the wake such as hairpin-like coherence structures (Figs. 9b3, 9c3, and 9c4). These coherent structures are also found in

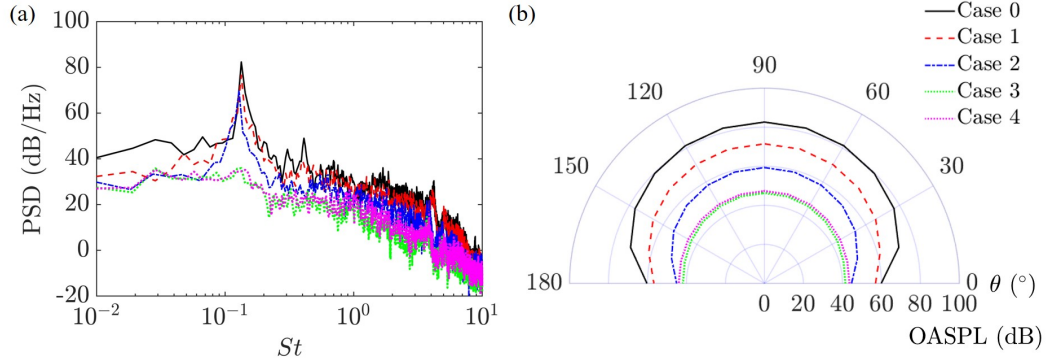


FIG. 7. Calculated far-field noise of wavy cylinders with different amplitudes. (a) PSD, (b) directivity. Case 0 (Straight), Cases 1–4 ($\lambda/D_m = 2.4$, $A/D_m = 0.10, 0.15, 0.20, 0.25$)

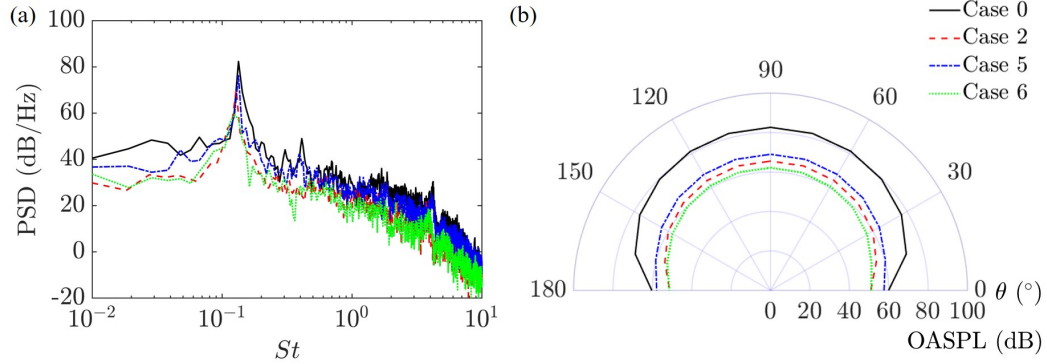


FIG. 8. Calculated far-field noise of wavy cylinders with different wavelengths. (a) PSD, (b) directivity. Case 0 (Straight), Cases 2, 5, 6 ($\lambda/D_m = 2.4, 4.0, 5.6$, $A/D_m = 0.15$)

previous works on wavy cylinders cylinders^{12,25}. This kind of distribution from spanwise vortex to streamwise and transverse vortex makes shear layers difficult to roll up large-scale spanwise coherent structures, which account for the noise reduction in Figs. 7 and 8.

Profiles of the time-averaged streamwise velocity \bar{u} along the streamwise direction is shown in Fig. 10. As expected, \bar{u} first decreases indicating a recirculation zone in the near wake. It then gradually recovers to the benchmark straight cylinder case. The distance between the cylinder centre and the location where $\bar{u} = 0$ defines the recirculation bubble length L_r ³⁹. Fig. 10(a) shows that for every wavy cylinder studied, the spanwise-averaged L_r exceeds that of the straight cylinder. It can also be observed that wave amplitude A has a greater impact than wavelength λ on the profiles. With increasing A from $0.10D_m$ to $0.20D_m$ (Cases 1–3), the reversal flow region is significantly stretched. The spanwise-averaged L_r increases up to $4.03D_m$ compared with $1.05D_m$ for the straight cylinder. When the amplitude increase from $0.20D_m$ to $0.25D_m$, the L_r will slightly decrease. However, the increment of reversal flow region is not obvious at constant A , except for the largest λ of $5.6D_m$ (Case 6). Additionally, Figs. 10(b) and 10(c) demonstrate that L_r in the saddle plane is longer than that in the node plane, consistent with previous studies^{19,20}.

In this study, the velocity fluctuation is stronger in the transverse component v than the streamwise component u , which is typically observed for vortex shedding from cylinders. Hence the vortex formation length L_f is defined at the location of maximum rms transverse velocity fluctuation v'_{rms} , both of which are crucial factors to influence the far-field noise. In Fig. 11(a), it can be observed that wavy cylinders exhibit a reduction in maximum v'_{rms} compared to the straight cylinder, and the vortex formation region is extended further downstream. With increasing A from Case 1 to 4, the maximum v'_{rms} value decreases and L_f increases. Even for both Case 3 and 4, it is hard to distinguish the peak from velocity profile. While for constant A (Cases 1, 5 and 6), a significant reduction of v'_{rms} occurs at $\lambda/D_m = 5.6$ (Case 5). These findings agree with the far-field noise reduction as shown in Figs. 7 and 8.

The variation of spanwise-averaged L_f shown in Fig. 11(a) is opposite to that of \bar{C}_D in Table IV, which agrees with the previous observation by Bearman⁴⁴. As illustrated in Figs. 11(b) and 11(c), the maximum v_{rms} in the node plane is larger than that in the saddle plane except Case 6. This suggests that the wake flow of most wavy cylinders exists more fluctuation in the node plane. In addition for Case 1, there shows a significant reduction of the maximum v'_{rms} in the saddle plane

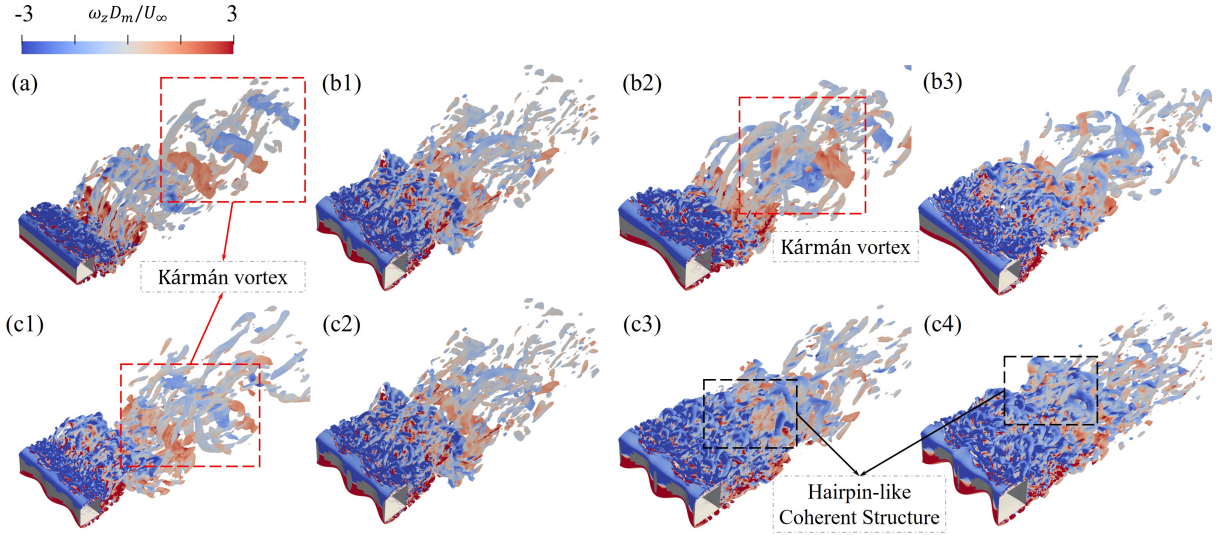


FIG. 9. Iso-surface of $Q_n = 0.5$, coloured by normalised spanwise vorticity, $\omega_z D_m / U_\infty$. (a) Straight cylinder, (b1–b3) Cases 2, 5, 6 ($\lambda/D_m = 2.4, 4.0, 5.6, A/D_m = 0.15$), (c1–c4) Cases 1–4 ($\lambda/D_m = 2.4, A/D_m = 0.10, 0.15, 0.20, 0.25$).

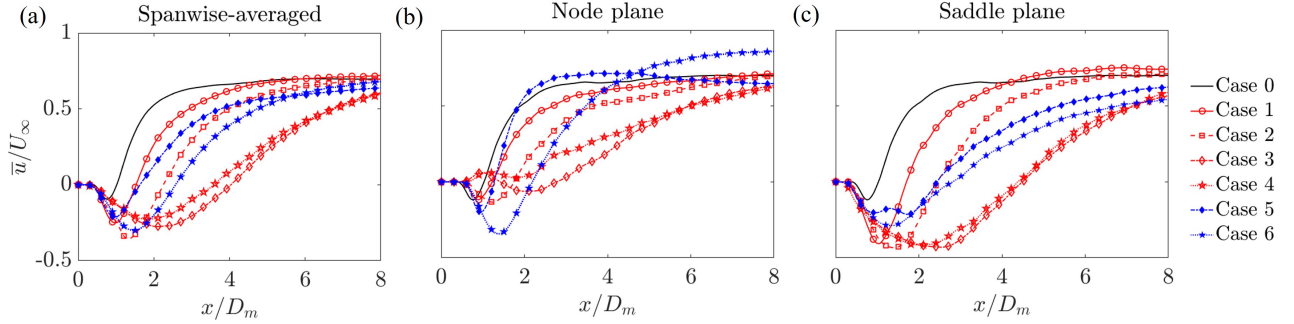


FIG. 10. Profiles of time-averaged streamwise velocity \bar{u} for the straight and wavy cylinders. (a) spanwise-averaged, (b) node plane, (c) saddle plane. Case 0 (Straight), Cases 1–4 ($\lambda/D_m = 2.4, A/D_m = 0.10, 0.15, 0.20, 0.25$) and Cases 2, 5, 6 ($\lambda/D_m = 2.4, 4.0, 5.6, A/D_m = 0.15$)

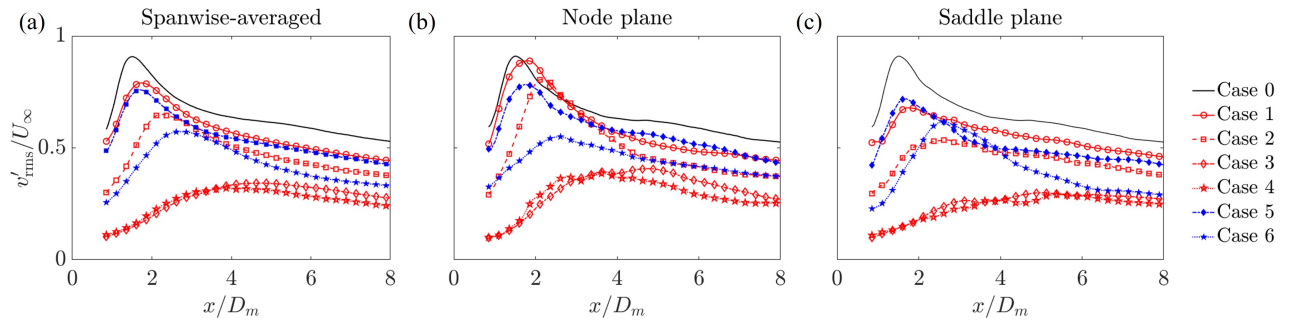


FIG. 11. Profiles of the rms transverse velocity v_{rms} for the straight and wavy cylinders. (a) spanwise-averaged, (b) node plane, (c) saddle plane. Case 0 (Straight), Cases 1–4 ($\lambda/D_m = 2.4, A/D_m = 0.10, 0.15, 0.20, 0.25$) and Cases 2, 5, 6 ($\lambda/D_m = 2.4, 4.0, 5.6, A/D_m = 0.15$)

but only a slight reduction in the node plane, which is consistent with the tonal noise characteristics (Fig. 8a). It can thus be inferred that node planes contribute more to far-field noise radiation.

Wall pressure fluctuations are the main source of aerodynamic noise from cylinder vortex shedding, which can be in-

ferred from the distribution of spanwise vorticity ω_z . Fig. 12 presents the contours of normalised time-averaged vorticity ($\omega^* = \bar{\omega}_z D_m / U_\infty$). In comparison with the straight cylinder where the two separated shear layers are symmetric about the centreline and relatively short, wavy cylinders exhibit elongated shear layers along the entire span, indicating a larger

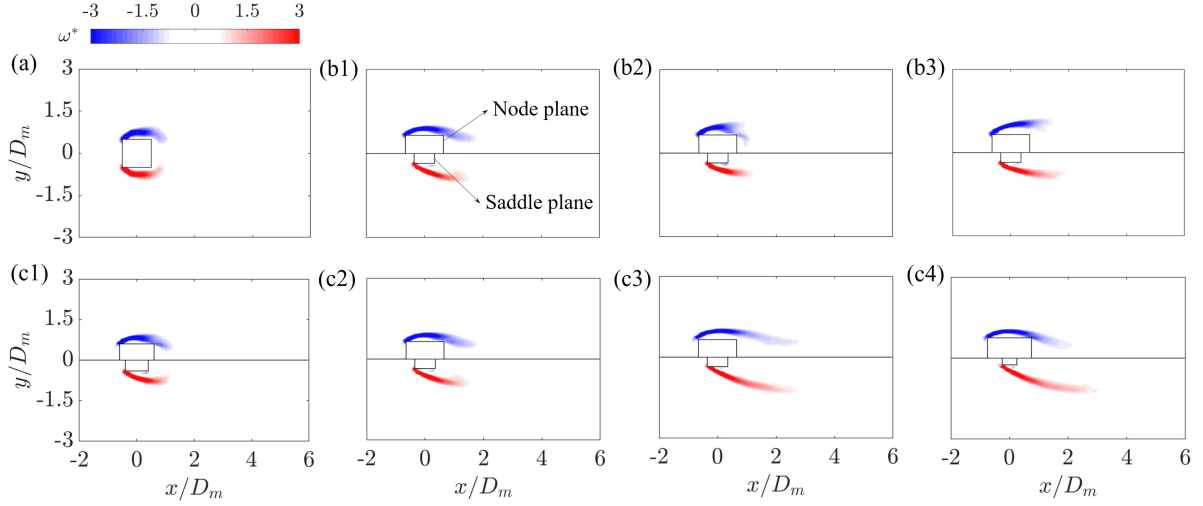


FIG. 12. Contours of normalised time-averaged spanwise vorticity. (a) straight cylinder, (b1–b3) Cases 2, 5, 6 ($\lambda/D_m = 2.4, 4.0, 5.6$, $A/D_m = 0.15$), (c1–c4) Cases 1–4 ($\lambda/D_m = 2.4$, $A/D_m = 0.10, 0.15, 0.20, 0.25$).

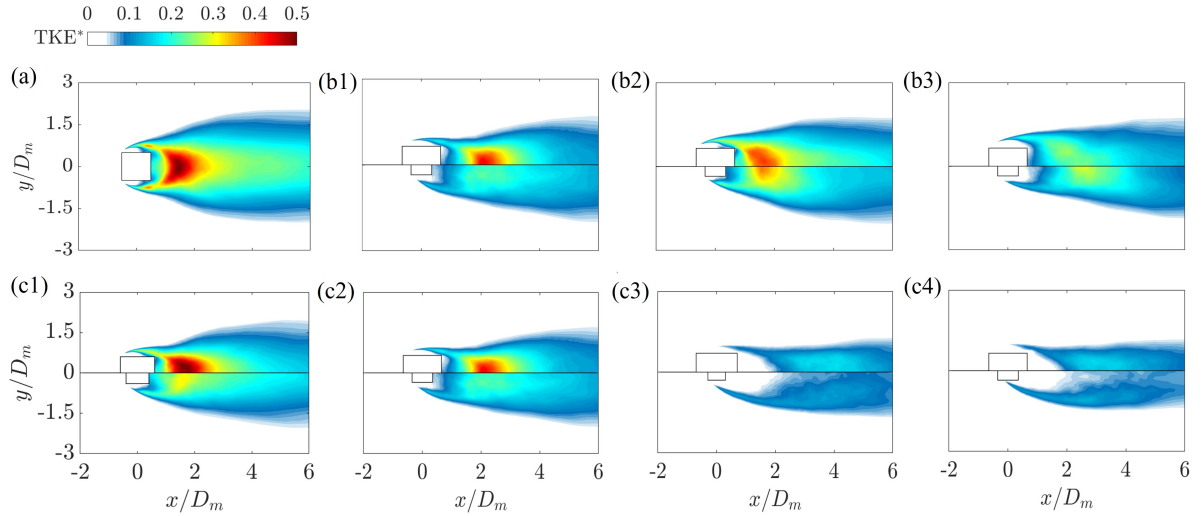


FIG. 13. Contours of normalised turbulent kinetic energy. (a) straight cylinder, (b1–b3) Cases 2, 5, 6 ($\lambda/D_m = 2.4, 4.0, 5.6$, $A/D_m = 0.15$), (c1–c4) Cases 1–4 ($\lambda/D_m = 2.4$, $A/D_m = 0.10, 0.15, 0.20, 0.25$).

vortex formation length L_f and diminished mutual interaction. This leads to weakened pressure fluctuations on the cylinder wall as well as in the near wake and hence the reduced far-field tonal noise.

This noise reduction mechanism is similar to those of some other noise control methods, such as air blowing on aerofoils^{45,46}. It can be observed in Fig. 12 that generally the shear layers of wavy cylinders are longer than those of the straight cylinder. In Figs. 12(c1)–12(c3), it is clear that the length of shear layer increases monotonically with the wave amplitude A . The shear layer length maximises in Case 3 (c3), which corresponds to the greatest noise reduction as shown in Fig. 7. Dependence of shear layer length on the wavelength λ is presented in Figs. 12(c1)–12(c3), which is non-monotonic, showing an order of shear layer length as Case 6 (b3) \approx Case

2 (b1) $>$ Case 5 (b2). Notably, although the shear layers are longer in Case 2 (b1, c2) than in Case 0 (a), the downstream ends of the top and bottom shear layers appear closer to the centreline at $y = 0$, which enhances pressure fluctuations in the near wake region. This also explains the different noise reduction effect shown in Fig. 8, albeit similar shear layer lengths in Case 2 (b1) and in Case 6 (b3).

Contours of normalised turbulent kinetic energy in the wake, $TKE = (u'^2 + v'^2 + w'^2) / (2U_\infty^2)$, are presented in Fig. 13. The maximum TKE occurs at the location of L_f as expected. Comparing with the straight cylinder, TKE values of the wavy cylinders are attenuated in both the node and saddle planes, and therefore expectedly in every spanwise plane, in line with the observed reductions in \bar{C}_D and $C_{L,rms}$ ⁴⁷. Additionally, TKE shows higher intensity in the node plane than

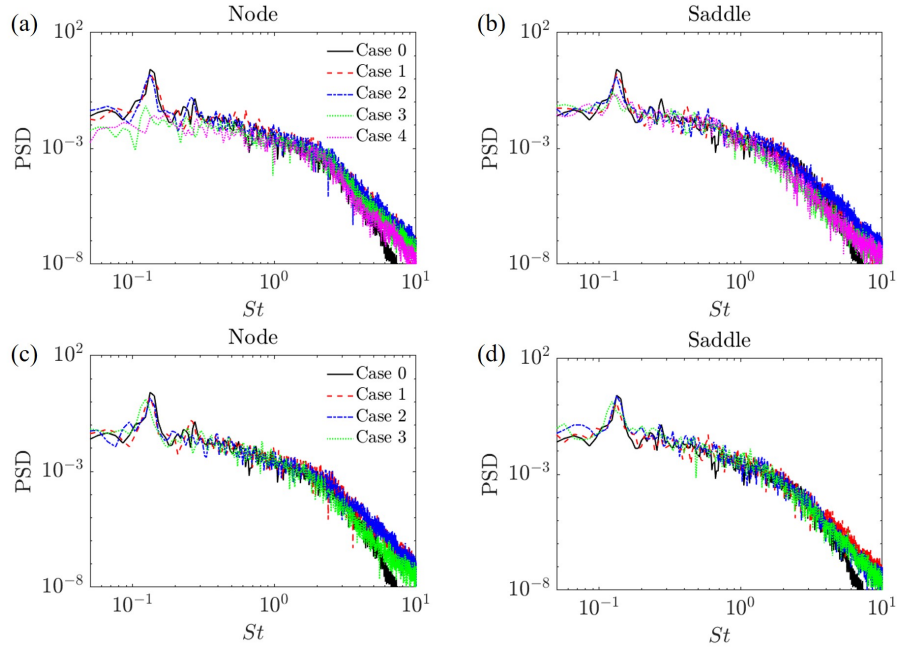


FIG. 14. PSD of transverse velocity fluctuation v' in the node and saddle plane. (a, b) Case 0 (straight), Cases 1–4 ($\lambda/D_m = 2.4$, $A/D_m = 0.10, 0.15, 0.20, 0.25$), (c, d) Cases 2, 5, 6 ($\lambda/D_m = 2.4, 4.0, 5.6$, $A/D_m = 0.15$).

in the saddle plane, indicating the presence of a distinct spanwise flow motion downstream of the cylinders, as a result of the introduction of a spanwise wavy shape²⁶. This spanwise TKE inhomogeneity disrupts the coherent vortex structures, which explains the relative noise contributions between the node and saddle planes, as discussed in Fig. 11.

For cylinders with the same wavelength λ in Figs. 13(c1)–13(c4), maximum TKE decreases with increasing wave amplitude A and remains unchanged from $A/D_m = 0.20$ – 0.25 . The maximum TKE reductions occur for Case 3 (c3) which reach 66% and 74% in the node and the saddle planes, respectively, relative to the straight cylinder. Notably, Case 2 (b1) exhibits higher TKE levels compared to Case 6 (b3), supporting the observation of stronger shear layer interaction in Fig. 12(b1). For Case 6 (b3), a remarkable TKE reduction in the near wake is observed, with the maximum TKE reductions in the node and the saddle plane as 46% and 42%, respectively. The maximum TKE indicates the dominant turbulence fluctuation in the near wake. In the near wake region, the high frequency turbulence fluctuation contribute to the broadband noise in the far field⁴⁸. Therefore for wavy cylinders the reduction of TKE in the near-wake region can explain the reduction of far-field noise PSD in the broadband frequency range^{26,45}.

To clearly illustrate the vortex shedding in both the node and saddle planes, the spectral analysis of transverse velocity fluctuation v' is performed as shown in Fig. 14. The probes are sampled in the cylinder wake at $(3D_m, D_m)$ in both the node and saddle planes. The primary peak occurs at the vortex shedding frequency, which is associated with the large-scale vortex shedding. Compared to the straight cylinder, the primary peak of the wavy cylinders are all reduced, which implies that the large-scale oscillation in the wake is suppressed

by the spanwise waviness, resulting in an attenuation of surface pressure fluctuations (dipole source) and thus the scattering of acoustic waves from near field to far field⁴⁹. In addition, there is no difference of vortex shedding frequency between the node and saddle plane. The vortex shedding frequency is consistent with the peak frequencies in the noise results of Figs. 7 and 8, which implies that the spectral characteristics of vortex shedding are similar in both the node and saddle planes.

Spanwise coherence of vortex structures in the wake flow, which is closely related to far-field noise, can be quantified by sampling velocity signals at two locations along the span¹², i.e.,

$$\gamma_{u_1 u_2}^2(\Delta z, f) = \frac{|\phi_{u_1 u_2}(f)|^2}{\phi_{u_1 u_1}(f)\phi_{u_2 u_2}(f)}, \quad (19)$$

where $\phi_{u_1 u_1}$ and $\phi_{u_2 u_2}$ are the auto-PSDs of streamwise velocity fluctuations u'_1 and u'_2 , and $\phi_{u_1 u_2}$ is the cross-PSD between u'_1 and u'_2 .

The contours of $\gamma_{u_1 u_2}^2$ against the spanwise distance Δz and Strouhal number St are presented in Fig. 15. Flow velocity signals are sampled at $(3D_m, D_m, z)$ and the reference point is at $(3D_m, D_m, 0)$. For the straight cylinder, a strong coherence is evident around $St \approx 0.13$, i.e., the vortex shedding frequency, as illustrated in Figs. 7(a) and 8(a). The value of $\gamma_{u_1 u_2}^2$ gradually decreases with increasing wave amplitude A in Figs. 15(c1)–15(c4), especially for Case 4 (c4) where spanwise coherence is significantly attenuated, suggesting highly 3-D vortex structures and a massive reduction in tonal noise level. However, the wavelength λ does not show the same trend. For Cases 2, 5 and 6, Fig. 15 (b1–b3), the coherence $\gamma_{u_1 u_2}^2$ is attenuated compared to the straight baseline, which is

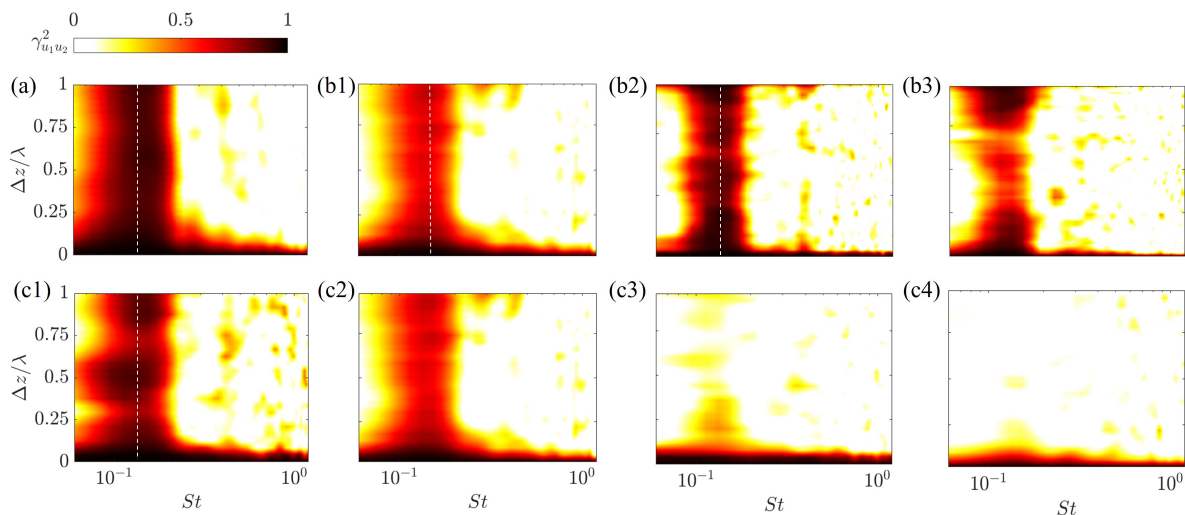


FIG. 15. Contours of spanwise coherence of streamwise velocity fluctuation. (a) straight cylinder, (b1–b3) Cases 2, 5 and 6 ($\lambda/D_m = 2.4, 4.0, 5.6, A/D_m = 0.15$), (c1–c4) Cases 1–4 ($\lambda/D_m = 2.4, A/D_m = 0.10, 0.15, 0.20, 0.25$). The white dashed line represents $St = 0.13$.

consistent with the tonal noise level shown in Fig. 8(a). As the wavelength λ increases from Case 1 (b1), the amplitude $\gamma_{u_1 u_2}^2$ first increases (Case 5, b2) and then drops significantly (Case 6, b3). These findings are consistent with the characteristics of near-wake flow and far-field noise. The spanwise waviness reduces velocity coherence at the point of separation, which causes the reduction of coherence in the wake, especially at vortex shedding frequency. This implies spanwise coherent structures of primary vortex are broken for wavy cylinders, which corresponding to tonal noise reduction in the spectrum.

IV. CONCLUSIONS

In the present study, numerical simulations were employed to investigate the aerodynamic noise radiated from sinusoidal wavy square cylinders at $Re = 2.2 \times 10^4$, considering different wave amplitudes ($A/D_m = 0.10, 0.15, 0.20, 0.25$) and wavelengths ($\lambda/D_m = 2.4, 4.0, 5.6$). To further investigate the noise reduction mechanisms, near-wake flow fields of these wavy cylinders were analysed. The amplitude and wavelength of wavy cylinders play a significant role in noise reduction. An increase in wave amplitude within the range of $A/D_m = 0.10$ – 0.20 leads to a gradual reduction in far-field noise. Specifically, at $A/D_m = 0.20$, tonal noise at $\theta = 90^\circ$ decreases significantly by 47 dB/Hz compared to the straight cylinder. When wave amplitude increases from $A/D_m = 0.20$ to $A/D_m = 0.25$, The noise remains nearly unchanged. Different wavelengths also exhibit notable noise reductions, with the maximum reduction of tonal peak by 23 dB/Hz for the wavelength of $\lambda/D_m = 5.6$. Moreover, substantial OASPL reduction occurs in multiple directions, with the maximum reduction in the lift direction and the minimum in the drag direction, which corresponds to a dipole-like directivity pattern.

Noise reduction mechanisms of wavy square cylinders

were investigated through the flow-field characteristics in the near wake. Wavy cylinders exhibit longer recirculation bubble length L_r and vortex formation length L_f compared to the straight cylinder, which suggests that vortex shedding is pushed further downstream. The maximum level of v'_{rms} in the node plane is larger than that in the saddle plane, indicating a spanwise flow motion in the wake. The analysis of flow structures reveals that large-scale vortex coherence structures of wavy cylinders become more 3-D and hairpin-like coherent structures emerge in the near wake. With increasing wave amplitude, the shear layer length is gradually extended and the interaction between the top and bottom shear layers is weakened compared to the straight cylinder. For wavy cylinders with the same wave amplitude, the maximum shear layer length occurs at the wavelength of $\lambda/D_m = 5.6$. The elongated shear layers indicate that vortex shedding is delayed, which accounts for the mechanism of reduction in tonal noise for the wavy cylinders. Simultaneously, turbulent kinetic energy in the wake is reduced remarkably, and the location of maximum TKE shifts downstream, which explains the reduction in broadband far-field noise. The spanwise coherence observed in the wake showed consistent effects of wave amplitude and wavelength on noise reduction.

Appendix A: Test for coefficient in WALE model

In this appendix, we investigate the influence of the coefficient C_w in the WALE model on the flow field results. The value of C_w is not universal. The typical value of C_w ranges from 0.325^{50,51}, the default value of FLUENT & OpenFOAM, to 0.5 as suggested by Nicoud and Ducros²⁹. However, the default value of STAR-CCM+ is 0.544, which is different from the typical values. Therefore, we choose three values of $C_w = 0.325, 0.440, \text{ and } 0.544$ to investigate the sensitivity of the solution to this coefficient. As shown in Fig. 16, the re-

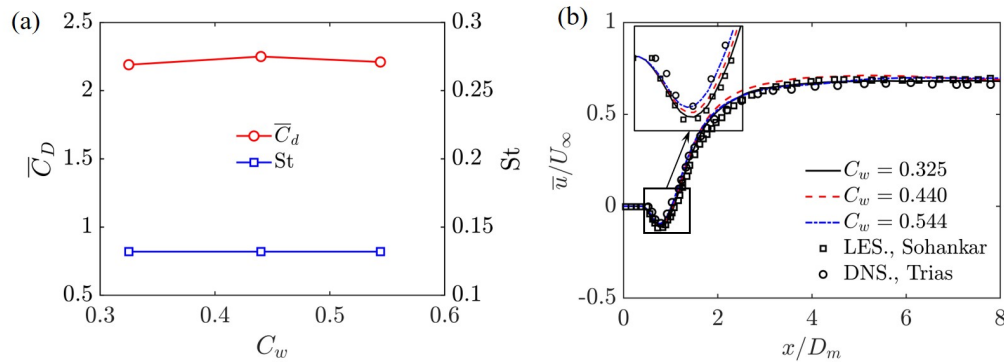


FIG. 16. (a) The variations of \bar{C}_D and St with different coefficient C_w . (b) profiles of time and spanwise averaged streamwise velocity \bar{u} for the straight with different coefficient C_w . Previous DNS (Trias et al.²⁷, $Re = 22000$) and LES (Sohankar et al.²⁸, $Re = 22000$) data of the straight cylinder are for comparison.

sults are insensitive to the C_w value within the WALE model. Therefore, in the present study the value of $C_w = 0.544$ (default value of STAR-CCM+) is reasonable to ensure accurate results.

ACKNOWLEDGMENTS

This research was supported by the National Natural Science Foundation of China (Grant Nos. 12111530102 and 12272163), the Natural Science Foundation of Shenzhen Municipality (Grant No. 20220814230752003), and the Royal Society International Exchanges (Grant No. IEC/NSFC/201061). The authors are grateful for the support from the Center for Computational Science and Engineering at Southern University of Science and Technology.

REFERENCE

- ¹D. J. Thompson, E. Latorre Iglesias, X. Liu, J. Zhu, and Z. Hu, "Recent developments in the prediction and control of aerodynamic noise from high-speed trains," *Int. J. Rail Transp.* **3**, 119–150 (2015).
- ²D. Lockard, M. Khorrami, M. Choudhari, F. Hutcheson, T. Brooks, and D. Stead, "Tandem cylinder noise predictions," in *13th AIAA/CEAS aeroacoustics conference (28th AIAA aeroacoustics conference)* (2007) p. 3450.
- ³Z. Li and J. Li, "Numerical simulation study of aerodynamic noise in high-rise buildings," *Appl. Sci.* **12**, 9446 (2022).
- ⁴F. O. Thomas, A. Kozlov, and T. C. Corke, "Plasma actuators for cylinder flow control and noise reduction," *AIAA J.* **46**, 1921–1931 (2008).
- ⁵C. Wang, H. Tang, S. Yu, and F. Duan, "Active control of vortex-induced vibrations of a circular cylinder using windward-suction-leeward-blowing actuation," *Phys. Fluids* **28** (2016).
- ⁶L. Shi, C. Zhang, J. Wang, and L. Ren, "Numerical simulation of the effect of bionic serrated structures on the aerodynamic noise of a circular cylinder," *J. Bionic Eng.* **9**, 91–98 (2012).
- ⁷Y. Xing, P. Liu, H. Guo, and L. Li, "Effect of helical cables on cylinder noise control," *Appl. Acoust.* **122**, 152–155 (2017).
- ⁸L. Li, P. Liu, Y. Xing, and H. Guo, "Experimental investigation on the noise reduction method of helical cables for a circular cylinder and tandem cylinders," *Appl. Acoust.* **152**, 79–87 (2019).
- ⁹T. F. Geyer, "Experimental evaluation of cylinder vortex shedding noise reduction using porous material," *Exp. Fluids* **61**, 1–21 (2020).
- ¹⁰E. J. Arcondoulis, T. F. Geyer, and Y. Liu, "An investigation of wake flows produced by asymmetrically structured porous coated cylinders," *Phys. Fluids* **33** (2021).
- ¹¹E. J. Arcondoulis, Y. Liu, Z. Li, Y. Yang, and Y. Wang, "Structured porous material design for passive flow and noise control of cylinders in uniform flow," *Materials* **12**, 2905 (2019).
- ¹²H. Bai, Z. Lu, R. Wei, Y. Yang, and Y. Liu, "Noise reduction of sinusoidal wavy cylinder in subcritical flow regime," *Phys. Fluids* **33** (2021).
- ¹³K. Lam and Y. Lin, "Large eddy simulation of flow around wavy cylinders at a subcritical reynolds number," *Int. J. Heat Fluid Flow* **29**, 1071–1088 (2008).
- ¹⁴Y. Lin, H. Bai, M. M. Alam, W. Zhang, and K. Lam, "Effects of large spanwise wavelength on the wake of a sinusoidal wavy cylinder," *J. Fluids Struct.* **61**, 392–409 (2016).
- ¹⁵H. Bai, M. M. Alam, N. Gao, and Y. Lin, "The near wake of sinusoidal wavy cylinders: Three-dimensional pod analyses," *Int. J. Heat Fluid Flow* **75**, 256–277 (2019).
- ¹⁶C. C. Zhang, W. Q. Wang, L. Shi, J. Wang, and L. Q. Ren, "Experimental and numerical study on aerodynamic noise reduction of cylindrical rod with bionic wavy surface," *Applied Mechanics and Materials* **461**, 690–701 (2014).
- ¹⁷P. W. Bearman and J. C. OWen, "Reduction of bluff-body drag and suppression of vortex shedding by the introduction of wavy separation lines," *J. Fluids Struct.* **12**, 123–130 (1998).
- ¹⁸J. Robichaux, S. Balachandar, and S. Vanka, "Three-dimensional floquet instability of the wake of square cylinder," *Phys. Fluids* **11**, 560–578 (1999).
- ¹⁹Y. Zheng, H. Rinoshika, D. Zhang, and A. Rinoshika, "Analyses on flow structures behind a wavy square cylinder based on continuous wavelet transform and dynamic mode decomposition," *Ocean Eng.* **216**, 108117 (2020).
- ²⁰D. Zhang, A. Rinoshika, Y. Zheng, Z. Li, and Y. Zhang, "Turbulent flow structures around a wavy square cylinder based on large eddy simulation," *Fluid Dynam* **57**, 96–110 (2022).
- ²¹A. Dobre, H. Hangan, and B. J. Vickery, "Wake control based on spanwise sinusoidal perturbations," *AIAA J.* **44**, 485–492 (2006).
- ²²A. A. Antiohos and G. R. Thorpe, "Effect of aspect ratio of a spanwise sinusoidal profile on the control of turbulent flows around bluff bodies," *J. Wind Energy Ind. Aerod.* **145**, 237–251 (2015).
- ²³A. Dobre and H. Hangan, "Investigation of the three-dimensional intermediate wake topology for a square cylinder at high reynolds number," *Exp. Fluids* **37**, 518–530 (2004).
- ²⁴R. M. Darekar and S. J. Sherwin, "Flow past a square-section cylinder with a wavy stagnation face," *J. Fluid Mech.* **426**, 263–295 (2001).
- ²⁵Y. Lin, H. Bai, and M. M. Alam, "The turbulent wake of a square prism with wavy faces," *Wind Struct.* **23**, 127 (2016).
- ²⁶X. Liu, Z. Hu, D. Thompson, and V. Jurdic, "Reduction of aerodynamic noise from square bars by introducing spanwise waviness," *J. Sound Vib.* **435**, 323–349 (2018).

- ²⁷F. X. Trias, A. Gorobets, and A. Oliva, “Turbulent flow around a square cylinder at reynolds number 22,000: A dns study,” *Comput. Fluids* **123**, 87–98 (2015).
- ²⁸A. Sohankar, L. Davidson, and C. Norberg, “Large eddy simulation of flow past a square cylinder: comparison of different subgrid scale models,” *J. Fluids Eng.* **122**, 39–47 (2000).
- ²⁹F. Nicoud and F. Ducros, “Subgrid-scale stress modelling based on the square of the velocity gradient tensor,” *Flow Turbul Combust* **62**, 183–200 (1999).
- ³⁰M. J. Lighthill, “On sound generated aerodynamically i. general theory,” *Proceedings of the Royal Society of London. Series A. Mathematical and Physical Sciences* **211**, 564–587 (1952).
- ³¹N. Curle, “The influence of solid boundaries upon aerodynamic sound,” *Proceedings of the Royal Society of London. Series A. Mathematical and Physical Sciences* **231**, 505–514 (1955).
- ³²J. E. Ffowcs Williams and D. L. Hawkings, “Sound generation by turbulence and surfaces in arbitrary motion,” *Philosophical Transactions of the Royal Society of London. Series A, Mathematical and Physical Sciences* **264**, 321–342 (1969).
- ³³Y. Cao and T. Tamura, “Large-eddy simulations of flow past a square cylinder using structured and unstructured grids,” *Comput. Fluids* **137**, 36–54 (2016).
- ³⁴S. Luo, M. G. Yazdani, Y. Chew, and T. Lee, “Effects of incidence and afterbody shape on flow past bluff cylinders,” *J. Wind Energy Ind. Aerod.* **53**, 375–399 (1994).
- ³⁵C. Norberg, “Flow around rectangular cylinders: pressure forces and wake frequencies,” *J. Wind Energy Ind. Aerod.* **49**, 187–196 (1993).
- ³⁶D. G. Crighton, “Basic principles of aerodynamic noise generation,” *Prog. Aerosp. Sci.* **16**, 31–96 (1975).
- ³⁷C. Wagner, T. Hüttele, and P. Sagaut, “Numerical method,” in *Large Eddy Simulation for Aeroacoustics* (Cambridge University Press, Cambridge, 2006) Chap. 5, pp. 267–237.
- ³⁸D. A. Lyn, S. Einav, W. Rodi, and J.-H. Park, “A laser-doppler velocimetry study of ensemble-averaged characteristics of the turbulent near wake of a square cylinder,” *J. Fluid Mech.* **304**, 285–319 (1995).
- ³⁹O. M. Griffin, “A note on bluff body vortex formation,” *J. Fluid Mech.* **284**, 217–224 (1995).
- ⁴⁰J. H. Seo and Y. J. Moon, “Aerodynamic noise prediction for long-span bodies,” *J. Sound Vib.* **306**, 564–579 (2007).
- ⁴¹H. Fujita, “The characteristics of the aeolian tone radiated from two-dimensional cylinders,” *Fluid Dyn. Res.* **42**, 015002 (2010).
- ⁴²J. Jacob and S. K. Bhattacharya, “Aerodynamic noise from long circular and non-circular cylinders using large eddy simulations,” *Int. J. Aeroacoust.* **21**, 142–167 (2022).
- ⁴³J. C. Hunt, A. A. Wray, and P. Moin, “Eddies, streams, and convergence zones in turbulent flows,” *Studying turbulence using numerical simulation databases, 2. Proceedings of the 1988 summer program* (1988).
- ⁴⁴P. Bearman, “Investigation of the flow behind a two-dimensional model with a blunt trailing edge and fitted with splitter plates,” *J. Fluid Mech.* **21**, 241–255 (1965).
- ⁴⁵J. Guo, R. Maryami, C. Yang, Y. Yang, X. Wang, and Y. Liu, “Aerodynamic noise reduction of a blunt flat plate by trailing-edge blowing,” *Phys. Fluids* **35** (2023).
- ⁴⁶C. Yang, E. J. Arcondoulis, Y. Yang, J. Guo, R. Maryami, C. Bi, and Y. Liu, “Active control of airfoil turbulent boundary layer noise with trailing-edge blowing,” *J. Acoust. Soc. Am.* **153**, 2115–2115 (2023).
- ⁴⁷W. Zhang, Daichin, and S. J. Lee, “Piv measurements of the near-wake behind a sinusoidal cylinder,” *Exp. Fluids* **38**, 824–832 (2005).
- ⁴⁸R. Maryami and Y. Liu, “Cylinder flow and noise control by active base blowing,” *J. Fluid Mech.* **985**, A10 (2024).
- ⁴⁹R. Maryami, E. J. Arcondoulis, and Y. Liu, “Flow and aerodynamic noise control of a circular cylinder by local blowing,” *J. Fluid Mech.* **980**, A56 (2024).
- ⁵⁰Z. Zhao, J. Wang, Y. Gong, and H. Xu, “Large eddy simulation of flow and separation bubbles around a circular cylinder from sub-critical to super-critical reynolds numbers,” *J. Mar. Sci. Eng.* **22**, 219–231 (2023).
- ⁵¹S. Qin, M. Koochesfahani, and F. Jaber, “Large eddy simulations of unsteady flows over a stationary airfoil,” *Comput. Fluids* **161**, 155–170 (2018).



Citation on deposit: Bao, H., Gan, L., & Liu, Y. (in press). Numerical study on aerodynamic and aeroacoustics characteristics of sinusoidal wavy square cylinders. *Physics of Fluids*

For final citation and metadata, visit Durham

Research Online URL: <https://durham-repository.worktribe.com/output/2949037>

Copyright statement: This accepted manuscript is licensed under the Creative Commons Attribution 4.0 licence.

<https://creativecommons.org/licenses/by/4.0/>